Chemical Science

ROYAL SOCIETY OF CHEMISTRY

EDGE ARTICLE

View Article Online
View Journal

Cite this: DOI: 10.1039/d6sc00456c

All publication charges for this article have been paid for by the Royal Society of Chemistry

Geometric orthogonality as a recipe for efficient intramolecular charge generation in core substituted NDI derivatives

Hugh C. Britton,†*[ab] Alberto M. Santa Daría,†[c] Chao Lyu,†[b] Andras B. Augusztin,[b] Lewis M. Cowen,[b] Dejan-Krešimir Bučar,[b] Alethea B. Tabor,[b] Bob C. Schroeder,[b] Sandra Gómez *[d] and Jose M. Marin-Beloqui *[ef]

One of the primary drawbacks of organic materials, compared to their inorganic counterparts in various optoelectronic applications, is their lower charge generation efficiency, which stems from their inherently higher exciton binding energy. Therefore, new out-of-the-box approaches need to be introduced to the field. Herein, we propose a new approach to increase the charge formation of naphthalenediimide (NDI) derivatives by inducing a large torsional angle between the NDI core and the core-attached substituent, deconjugating the resulting extended π-system. To study the extent of this change, transient absorption spectroscopy characterisation has been performed on a set of derivatised NDI molecules where the core-attached substituents have been systematically altered to modulate the resulting torsional angle. The data indicates an enhanced charge generation with core-attached substituents from phenyl to anthracenyl which increase in both size and degree of rotational inhibition. State-of-the-art excited state simulations using the TD-B3LYP/def2-SVP level of theory were performed to calculate absorption spectra and to parametrise potential energy surfaces to run non-adiabatic quantum dynamics simulations for the two extreme NDI systems, showing crucial differences due to the influence of charge transfer states. This opens the possibility for a new family of NDI molecules with implications for a wide range of applications such as photovoltaics, transistors and catalysis.

Received 16th January 2026
Accepted 26th March 2026

DOI: 10.1039/d6sc00456c

rsc.li/chemical-science

Introduction

The transfer of electrons is at the heart of a myriad of chemical and physical processes such as photosynthesis, radical reactions, catalysis and organic electronics. However, most organic materials lack the ability to efficiently generate charges upon external stimuli, particularly by photoexcitation. The main reason for this low efficiency is the large exciton binding energy, which hinders the separation of the singlet exciton into free charges. This is a major reason why organic materials, despite their obvious advantageous properties such as flexibility, transparency, and low-cost manufacturing, have not been widely adopted.

Efficient generation of charges in organic materials typically relies on using two materials, with one serving as the donor and the other as the acceptor.[1–3] But the use of two different materials is accompanied by a myriad of associated problems such as poor miscibility,[4] lack of morphology control,[5] energy losses[6] and stability.[7] These problems highlight the utmost importance of new approaches to generate charges and thus obtain organic molecules able to yield free charge carriers without the need for a second material.

To this end, we conduct a detailed investigation of the excited state dynamics, focusing on charge generation enabled by the orthogonality between a central naphthalenediimide (NDI) core and its substituents. The NDI core was selected as it is a building block commonly used in literature due to its ability to generate negative charges. This ability, paired with its outstanding oxidative stability, has granted it a large presence in the field of organic photovoltaics and field effect transistors.[8–13] Numerous strategies aimed at enhancing the charge generation in NDI molecules have focused on the substitution at the imide nitrogen.[14–17] In instances where substituents have been attached to the NDI naphthalene core, prevalent approaches have predominantly employed electron donating moieties such as thiophenes and amines to facilitate charge generation by raising their highest occupied molecular orbital (HOMO) level.[18–22] This

[a]School of Chemistry and Chemical Engineering, University of Southampton, Southampton, SO17 1BJ, UK. E-mail: H.C.Britton@soton.ac.uk
[b]Department of Chemistry, University College London, London, WC1 0AJ, UK
[c]Universidad de Salamanca, Pl. de los Caídos s/n, 37008 Salamanca, Spain
[d]Department of Chemistry, Module 13, Universidad Autónoma de Madrid, 28049 Madrid, Spain. E-mail: sandra.gomezr@uam.es
[e]Department of Physical Chemistry, University of Malaga, Andalucia-Tech Campus de Teatinos s/n, 29071 Málaga, Spain. E-mail: jm.marinbeloqui@uma.es
[f]Materials and Nanotechnology College Institute (IMANA), University of Malaga, Campus de Teatinos s/n, 29071 Málaga, Spain
† These authors contributed equally.

reliance has been rooted in electronic effects, diverging from our geometric approach, to decrease the electronic coupling between the core and the substituents. Literature provides an instance in which an anthracene moiety is conjugated to the NDI core; however, an amine functional group is also affixed to the NDI core. Consequently, the predominant contribution to charge generation is attributed to the donor characteristics of the amine group, rather than the anthracene substituent.[23] Other examples of NDI core substitution found in literature focus on the attachment of halogen substituents to the NDI core to induce triplet formation by an increase of the spin–orbit coupling through the heavy atom effect.[23,24] However, the effects of attaching diverse aromatic groups to the NDI core on the geometry and charge generation have not previously been explored.

Charges generated by the molecules presented in this work offer a distinct advantage over other examples in literature where orthogonal charge formation is shown. In their vast majority, such charges are formed either in larger molecules like polymers,[25] where the charge separation is more accessible than in a small molecule, or through strong donor units, again relying on electronic effects.[23,26] Accordingly, Wu *et al.* published a work where they synthesise a strong donor character unit of indacenodithiophene (IDT) sandwiched between two orthogonal NDI units with the ability to generate charges.[27] However, the IDT unit large donor strength makes impossible to isolate the role of orthogonality in the charge generation process. In our work, the charge generation occurs in small single-molecules with the orthogonality between the main NDI core and the core substituent as the main relevant actor.

Herein we report a series of NDI core substituted molecules with large aromatic substituents. We synthesised a series of five NDI analogues – **NDI-Ph** (phenyl), **NDI-Th** (thiophenyl), **NDI-Mes** (mesityl), **NDI-Nap** (naphthalenyl) and **NDI-An** (anthracenyl) – with a range of aromatic groups of differing sizes (Scheme 1). We anticipated that as the size of the aromatic moieties increased, the steric hindrance between the NDI and the flanking substituents would also increase, thus inducing a larger orthogonality and reduced π-orbital overlap. Furthermore, in some cases configurationally stable biaryl atropisomers could result, particularly for large analogues or with large *ortho*-substituents. The core substitution with larger aromatic moieties introduces a significant steric hindrance between the substituent and the imide carbonyls, resulting in a nearly orthogonal torsional angle between both aromatic units and a dramatically reduced π-orbital overlap.

Unravelling the identity of the charged states observed in the different NDI derivatives upon excitation, presents a challenge. The main reason for this is that the differences between charge transfer and separated charge states are often minimal in terms of their spectral characteristics.[28] Results indicate, however, that we cannot associate these charges to twisted intramolecular charge transfer (TICT) states. Molecules that undergo TICT change their ground state geometry, upon excitation, to a twisted geometry in favour of a more energetically favourable charge transfer (CT) state.[29–31] The NDI derivatives herein presented maintain their orthogonality in ground and excited states. CT generation in TICT molecules are very solvent sensitive, as the viscosity and intermolecular interactions play a major role in the geometry evolution upon excitation.[32,33] Although some TICT systems can exhibit ultrafast charge transfer, their dynamics generally rely on significant excited-state geometry relaxation, which can constitute an efficiency loss pathway, unlike the largely rigid orthogonal structures studied here.

Transient absorption spectroscopy (TAS) was chosen to characterise the charge generation process in the presented series of NDI derivatives. In short, TAS is a technique with two different light sources, where one excites the sample whereas the other one probes the photogenerated excited species. Moreover, creating a delay between the two light sources is possible to obtain information about the time evolution of the photogenerated excited species. This technique is widely used in the field to study the excited state behaviour in organic molecules[34,35] as the TAS signal is proportional to the number of charges created due to the Beer–Lambert law.[36–38]

The implications of the geometric orthogonality approach for charge generation extend beyond applications where charges are the ultimate goal, such as catalysis, photovoltaics, and transistors. Charges also serve as key intermediates in processes like singlet fission, thermally activated delayed fluorescence, and triplet formation, enabling diverse applications including LEDs and bioimaging.[39–42]

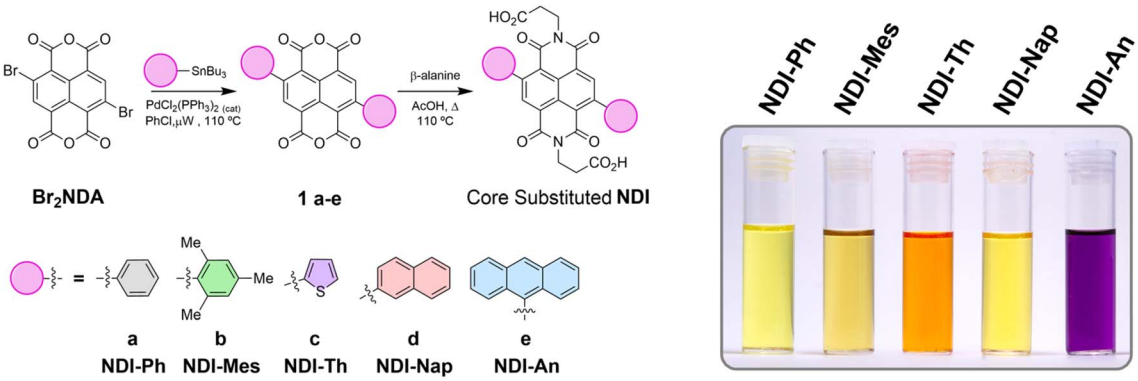

Scheme 1 Synthesis of core-substituted NDI dicarboxylic acids **NDI-Ph**, **NDI-Mes**, **NDI-Th**, **NDI-Nap** and **NDI-An**. Insert shows the range of colours of the final products.

Results

Synthetic procedures

As limited studies have previously been reported on aromatic core-substituted NDIs, it was necessary to develop a flexible and robust synthetic route that would deliver the NDI analogues in good yield and high purity. Initially the syntheses of the substituted NDIs were attempted by reacting known dibromide dianhydride **Br_2NDA** with β-alanine in AcOH to give imide **Ala_2NDI** in >70% (SI Scheme S1).[43–45] Unfortunately, **Ala_2NDI** was highly insoluble in all organic solvents, preventing subsequent introduction of aryl substituents directly to the NDI core *via* standard Pd-mediated approaches. This was attributed to well-known insolubility of NDI core substrates exacerbated by the carboxylic acid side chains (chosen to allow subsequent NDI functionalisation for a variety of applications).[10,46–48]

This necessitated a change in the synthetic approach. The anhydride core **Br_2NDA** was observed to be notably more soluble in a range of organic solvents. However, the sensitive anhydride and bromide functionalities precluded the use of bases in coupling reactions and attempted coupling under standard Suzuki and Sonagashira conditions resulted in decomposition and byproducts.[49,50] On the other hand, the neutral Stille reaction conditions provided a viable solution to this issue and following precedent, microwave coupling conditions at high temperature to aid solubility, delivered known **1a** and the novel anhydrides **1b–e** in 51–95% yields.[51–55] The aromatic core-substituted NDI anhydrides **1a–e** were highly coloured, most notably a brilliant purple for **1e** containing flanking anthracene units. In the final step, the desired imide was introduced through condensation with β-alanine to yield **NDI-Ph**, **NDI-Mes**, **NDI-Th**, **NDI-Nap** and **NDI-An** in 66–88% yields spanning a similar range of vibrant colours.

Spectroscopic analysis

Fig. 1 shows the ground state absorbance of the various NDI derivatives in 2-methyltetrahydrofuran (2-MeTHF) solutions. It is possible to see the characteristic NDI core bands with little variations among them (375, 377 and 379 nm for **NDI-Ph**, **NDI-Nap** and **NDI-Th**, respectively). For **NDI-An**, the NDI core transitions are slightly obscured by the anthracene bands.

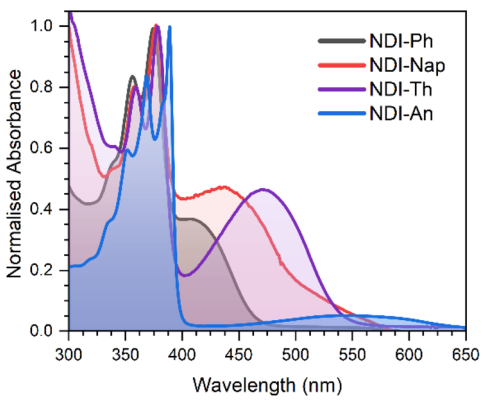

Fig. 1 Ground state absorbance of 2-methyltetrahydrofuran (2-MeTHF) solutions of NDI-Ph (black), NDI-Nap (red), NDI-Th (purple) and NDI-An (blue).

In addition, there is another band at longer wavelengths which is associated in literature with NDI CT bands.[15,23,56] We see a larger displacement to the red of this band when the size of the carbon-only substituent is increased phenyl < naphthalene < anthracene. The lower energy absorption band for the thiophene substituted molecule is positioned between the anthracene and the naphthalene. The presence of this longer wavelength band is in line with a more effective separation of the electronic distribution between HOMO and the lowest unoccupied molecular orbital (LUMO) levels, associated with CT states. This effective separation stabilises the LUMO and raises the HOMO levels, and, therefore, decreases the bandgap of this electronic transition.[57–59] The larger red-shift for **NDI-Th** can be explained firstly in light of the electron rich nature of the thiophene ring. This larger donor nature leads to more efficient orbital mixing with the electron deficient NDI core, resulting in a reduced optical bandgap. Secondly, due to the smaller five-membered thiophene ring, the steric hindrance between the thiophene and NDI core is reduced, leading to a more planar overall structure, facilitating electron delocalisation.

To confirm the assignment of these bands to CT states, we represented Mulliken dependence[60–62] of the CT frequency with the oxidation potential of the substituents obtained from literature[63–65] (Fig. S2). We have used oxidation potential since the NDI donor remains constant, and the oxidation potential represents a close measurement of the donor strength.[66] A linear dependence between the CT frequency and the oxidation potential is associated with an unequivocal CT nature of the corresponding absorption band.[67] However, as seen in our case, the dependence was not well fitted to a line, indicating that the charged species associated with these bands did not share the same origin. This deviation from linear dependence could be originated by a significant decoupling of the NDI core and the substituent. This decoupling is in line with the small displacement (0.03 eV from **NDI-Ph** to **NDI-Th**) seen for the NDI core bands in the ground state absorbance spectra.

To investigate this decoupling between the donor moiety and the acceptor NDI core, we performed cyclic voltammetry (CV) on the NDI compounds (see SI). The reduction of all five compounds led to the same electron affinity (EA), 3.8 eV, which we can approximate to the LUMO level. This EA is similar to other pristine-like NDI molecules in literature.[66] The results of the Mulliken dependence indicated that the obtention of the ionization potential from the EA and the bandgap would not be precise, since the CT band seems to be originated by different species. The same EA for all the molecules is consistent with a large decoupling between the NDI core and the substituent, or that it is just extended to the first couple of carbons of the substituent.

We then conducted photoluminescence (PL) studies (Fig. S3). Upon excitation at 365 nm, **NDI-Ph** and **NDI-Nap** exhibit a fluorescence band near 420 nm, along with a second emission band at *ca.* 550 nm observed for **NDI-Nap**, **NDI-An**,

and **NDI-Th**, while **NDI-Ph** lacks this red-shifted emission. This red-shifted emission intensifies with larger substituents.

While NDI derivatives are known to form aggregates that could influence optical properties, we confirmed the absence of such effects in our system. To exclude potential aggregation effects in our characterisation, we measured the absorbance of **NDI-An** (the paradigmatic system in this study) across a concentration range spanning two orders of magnitude, including the concentration where the further characterisation is performed (Fig. S3b). The spectra show no changes in the relative absorbance of the NDI core and the CT band, nor any baseline variations. This result confirms the absence of aggregation within the concentration range investigated along this work.

To better understand how the optical properties relate to charge behaviour, fs-TAS was performed in 2-MeTHF solutions. Fig. 2 shows the results with the smallest and the largest substituent, **NDI-Ph** and **NDI-An**, respectively. The **NDI-Nap** and **NDI-Th**, the intermediate size molecules are shown in the SI. Two different excitation wavelengths were selected for the TAS experiments: one matching the absorbance of the NDI core (at 375 nm) and the other one exciting the lower absorbance band associated to the CT transition (in the range of 420–550 nm).

Upon exciting **NDI-Ph** at 375 nm, a large band at 480 nm that extends in the 550–800 nm region with a broad absorption is observed. This band decays with a lifetime of 0.5 ps to leave only the broad band centred at 650 nm with a lifetime of 1.3 ns. Upon excitation of **NDI-Ph** at the band at 415 nm, a similar TA spectrum was obtained with identical bands (see Fig. 2a and b).

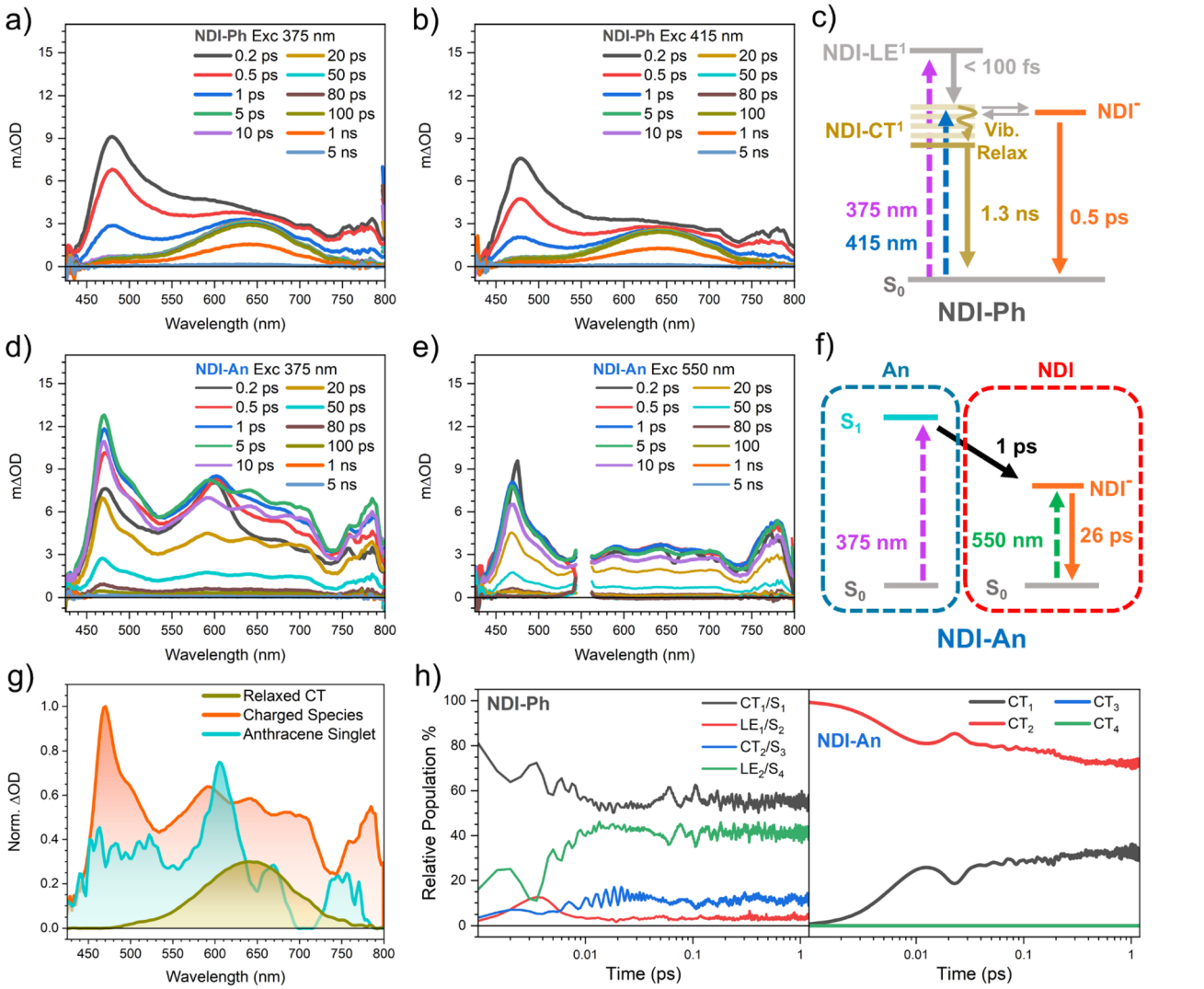

Fig. 2 Femtosecond transient absorption data of 2-MeTHF solutions of (a and b) **NDI-Ph** and (d and e) **NDI-An** upon excitation at (a and d) 375, (b) 415 and (e) 550 nm. Excitation density was maintained at 0.25 mW. Jablonski diagram of the excited state dynamics of (c) **NDI-Ph** and (f) **NDI-An** upon photoexcitation. (g) Decay Associated Spectra (DAS) of the species obtained by global analysis treatment of the ps-TAS data for all the molecules studied. (h) Percentage of decay of the initial electronic state after the pump/light irradiation of the low energy transition and percentage of other states over time in logarithmic scale for **NDI-Ph** (left) and **NDI-An** (right). Calculated using the wavepacket quantum dynamics method ML-MCTDH on TD-B3LYP precomputed potentials on full dimensionality.

On the other hand, upon excitation of **NDI-An** at 375 nm (Fig. 2d), where anthracene and the NDI core both absorb, a narrow band is observed at 600 nm at 0.2 ps. This 600 nm narrow band decays with a lifetime of 1 ps. In addition, there is a spectral feature with a band at 470 nm that extends into the infrared. This 470 nm feature rises at the same time the 600 nm band decays. This 470 nm band is almost identical to **NDI-Ph** TA spectrum at early times. However, in this case, the spectral feature at 470 nm is much more defined, with additional bands at 590, 638, 700 and 785 nm. When exciting the **NDI-An** band at 550 nm, only the defined feature with the 470 nm band is seen. Under both excitation wavelengths the defined 470 nm feature fully decays with a lifetime of 26 ps.

To help elucidate the photoexcitation mechanism we performed global analysis on the TA data for all the molecules studied (Fig. S2). This analysis provided three different species: a broad band centred at 650 nm, the multiband feature with the maximum absorbance at 470–480 nm and the narrow band at 600 nm. First, we can rule out the presence of triplet species as, their absorbance spectrum does not match ^{3}NDI absorbance in the literature, neither T_n nor T_1.[15,24,68] Also, the triplet lifetime is expected to be much larger (microsecond timescale) due to the forbidden triplet to singlet ground state transition. The defined multiband TA feature with its maximum at *ca.* 470 nm, is assigned to a NDI charged species due to its similarity to the NDI radical anion spectrum measured in literature.[15,69] Then, the next species, the sharp band at 600 nm can be either associated with the absorbance of the anthracene or NDI core singlet exciton due to its similarity to the anthracene[15,70,71] and pale NDI[24,72] singlet absorbance seen in literature.[15,68,69] The ground state absorbance of pristine NDI and anthracene molecules in the same region makes difficult to calculate the percentage of light absorbed by either unit. However, the similarity of the ground state absorbance of **NDI-An** to the anthracene absorbance, with that particular vibronic progression, we can infer that a larger portion of light is going to be absorbed by the anthracene unit. This larger absorption of the anthracene unit suggests the 600 nm band to be associated with the anthracene singlet. Finally, the global analysis provides a featureless broad band at 650 nm that does not appear for **NDI-An** which position is slightly displaced (0.16 eV) relative to the localised NDI singlet exciton seen in literature: a sharp band at 600 nm.[24,72] However, this state is accessible by excitation at lower energies **NDI-Ph** and **NDI-Nap**, confirming it does not originated from the pristine NDI core singlet. We instead assign this species to a relaxed singlet with a significant CT character. While the electronic density is primarily localised on the NDI core, it is expected to extend to the first carbon atoms of the phenyl and naphthalene substituents, in line with a larger coupling of these substituents and the NDI core (see in the Calculations section). The substantial CT character, combined with an extended conjugation facilitated by the substituent's carbon atoms, explains both the observed red shift and the broader spectral profile compared to the unsubstituted NDI singlet. The lifetime of this species, which matches the measured PL lifetime (Fig. S3), hence, suggests this species as the origin for the PL for **NDI-Ph** and **NDI-An**. The assignment for the PL to a state with a large CT character, as opposed to a localised state (LE), is in agreement with a less vibronically defined PL spectrum and the red-shift seen for our compounds in comparison to the pristine NDI PL seen in literature.[24,72] Therefore, we can safely assign our band at 650 nm to a relaxed singlet with a large CT character. Therefore, we hypothesise that upon excitation of the **NDI-Ph** at 375 nm, the NDI core singlet is swiftly, in less than 100 fs since it is not seen in the fs-TAS, transformed into a hot CT state. This hot CT state would be in equilibrium with the NDI charged species, but upon relaxation, this equilibrium is no longer possible. Then, this relaxed CT state decays into ground state with 1 ns lifetime. This relaxation in the ps timescale, which hinders the transfer to another state, agrees with other molecules seen in literature.[73,74] The direct excitation of the CT state, at 415 nm, populates the hot CT state, and the TA spectrum gave similar results. The **NDI-Nap** shows a similar trend to **NDI-Ph**, but **NDI-Nap** shows a lower weight of the hot CT state when excited at longer wavelengths (Fig. S5). This lower weight of the hot CT state is coherent with a more stable CT state given by the larger extension for the conjugation. In addition, it is possible to see a ps decay of the **NDI-Nap** relaxed CT state in line with a vibrational relaxation process. Therefore, the **NDI-Nap** data further supports the assignment of this 650 nm band to a relaxed CT state.

Following the assignment made in the last paragraph, the lack of NDI singlet excitons upon exciting **NDI-An** became apparent, while there is a considerable formation of singlet excitons, with large CT character, in **NDI-Ph**, with the **NDI-Nap** remaining as an intermediate case. In addition, this assignment also explains the differences seen for different excitation wavelengths for **NDI-An**: exciting the **NDI-An** anthracene moiety, the anthracene singlet exciton is formed, which is swiftly transformed into charged NDI moiety in the hundreds of femtosecond timescale. The fast generation of charges seen for all the molecules studied in this work is remarkable, but it is a sensible affirmation if we see other more conjugated NDI molecules in literature.[75–77] As discussed earlier, there appears to be a pattern in the charge generation depending on the substituent where the NDI derivative with the largest substituent, **NDI-An**, generates a larger portion of charges in comparison with the NDI derivative with the smaller phenyl substituent, **NDI-Ph**.

Theoretical calculations

We performed calculations to better understand the behaviour of these molecules. First, we have performed time-dependent density-functional theory (TD-DFT) calculations using TD-B3LYP-D3/def2-SVP method on all molecules. Interestingly, in all cases the LUMO orbital has exactly the same topology, strongly localised on the NDI core unit (Fig. S15 and S16). This is a clear indication of the decoupling of the NDI core and the substituent, and agrees with the experimental CV data, demonstrating the validity of the calculations. To quantify the electronic coupling associated with charge-transfer processes in the NDI-H simplified models, we employed the generalized

Mulliken–Hush (GMH) and fragment charge difference (FCD) schemes as implemented in Q-Chem (more information can be found in the SI). These calculations yielded electronic coupling values (H_{DA}, FCD/GMH) of 0.353/0.326 and 0.031/0.032 eV for **NDI-Ph** and **NDI-An**, respectively. As expected, these values correspond to the largest and smallest couplings among the series, respectively. Our calculated **NDI-Ph** coupling values completely match with others, calculated from experimental data, found in literature.[23] In contrast, in the same reference, Gurzadyan *et al.* find a coupling value for a structurally similar system to **NDI-An** that falls within the same range as our value for **NDI-Ph**. In their system, the intrinsic donor character of anthracene is masked by the more strongly donating amine substituent. Consequently, all their H_2N-NDI derivatives exhibit nearly identical ground-state absorption spectra, indicating the amine dominates the electronic properties. The low coupling value we calculate for **NDI-An** is, in fact, consistent with systems where coupling is deactivated by meta-substitution or orthogonal geometries, further validating the accuracy of our computational approach.[78–80]

To confirm the assignment done in the fs-TAS section, excited state simulations, upon excitation of the lowest energy band, were performed using the ORCA[81] and Q-Chem[82] software packages at the TD-B3LYP/def2-SVP level of theory. These calculations provided the necessary parameters for subsequent non-adiabatic quantum dynamics simulations. To perform non-adiabatic quantum dynamic calculations, the ML-MCTDH[83] method was used as implemented in the Quantics package,[84] after constructing potential energy surfaces based on linear vibronic coupling models (see SI for calculation details).[85,86] As shown in Fig. 2h, **NDI-Ph** showed the presence of LE singlet states alongside CT states whereas **NDI-An** showed only CT states. **NDI-Ph** shows a dependent exchange of two different states, namely S_1 and S_4, with LE and CT character, respectively, which represent the largest population in the first femtoseconds (95% of the population upon excitation). According to the topology of this S_1 state (π_{AQbenz}, Fig. S11), the CT character is not that pronounced as for **NDI-An**, which agrees with the relaxed CT state seen in fs-TAS. In addition, there is a certain population of a purer CT character (HOMO strongly localised over the phenyl group) state, S_3, which can be associated with the charged species seen in the fs-TAS. On the other hand, there is only two singlets, with CT character, with enough population on the calculated dynamics of **NDI-An**, which interconvert one into another (CT_1 and CT_2). Then, according to these calculations CT_1 and CT_2 coexist in the first picosecond, but the CT_2 is transforming into the CT_1. According to the topology of these states (Fig. S14), the CT_1 and CT_2 are very similar, with most of the electronic density localised over the anthracene moiety, but CT_1 shows the anthracene accommodating the positive charge with the NDI core oxygen through space. Therefore, the dynamics seen for **NDI-An** upon excitation of the CT band show the excitation of the anthracene moiety to then stabilise the positive charge through space with the NDI oxygen. Interestingly, despite finding isoenergetic triplet energy levels in our calculations (Fig. S17), the calculated dynamics did not show any population in the picosecond timescale of triplet states unlike in other NDI derivatives from literature.[24] Spin–orbit coupling (SOC) calculations on **NDI-Ph** and **NDI-An** (Fig. S18) confirm the lack of triplet state population due to a very low SOC between excited singlet and triplet states.

Crystallographic structural analyses

The differences in excited state dynamic with the substituent size led us to further study their molecular structure using single crystal X-ray diffraction analyses, which was then further probed using computational approaches (see the Discussion section). Single crystals of **NDI-Th**, **NDI-Ph** and **NDI-An** were grown through solvent diffusion of diethyl-ether into THF solutions of the NDI derivatives. X-ray diffraction studies have shown that **NDI-Th** and **NDI-Ph** crystallise as isomorphous THF solvates in the monoclinic $P2_1/n$ space group. The crystallisation of **NDI-An** resulted in the concomitant formation of two solvates – a diethyl-ether solvate and a diethyl-ether-THF solvate. Both crystallise in the triclinic $P\bar{1}$ space group (see Section 6 in the SI document).

In all crystal structures, the NDI derivatives feature a non-planar conformation with various degrees of tilting between the NDI core and the flanking substituents. Specifically, the disordered thiophenyl groups in **NDI-Th** are tilted about 69° (in both occupancy sites), the phenyl groups in **NDI-Ph** flank the NDI core at a 65° angle, while the anthracenyl groups in both discovered **NDI-An** crystal forms assume angles in the range of 84–88°, almost perpendicular to the NDI core (Fig. 3). We note that no crystal form screens have been pursued to evaluate the existence of NDI derivatives with 'flat' molecular structures. But based on the crystallographic and computational analyses, we reason that, in the solid state, the studied NDI derivatives (and particularly those with bulkier substituents) favour more orthogonal arrangements of the NDI core and the substituent. It is therefore, expected that, in solution, the media where the spectroscopic characterisation has been made, the orthogonal conformation still persists. The largely orthogonal conformation of the studied molecules is consistent with the charge generation discussed previously. Free rotation, with a subsequent increase of electronic coupling, would reduce free charge generation efficiency and/or increase charge recombination losses.

Discussion

To calculate the extent of the orthogonality impact in the charge generation, further calculations were performed to quantify the steric hindrance of the substituent on these molecules (Fig. 4a). The calculations show the expected behaviour with a larger rotational energy barrier with a larger substituent. Interestingly, the calculated potential scan is not fully symmetrical. This is due to the rapid localisation of the electronic density on one of the oxygens, and therefore creating an asymmetry in the NDI core. That is also the reason why the energy minimum, for instance, for the **NDI-Ph**, is not exactly zero but around 60° (matching the XRD data). Of all the NDI derivatives, the **NDI-Th** displayed the lowest rotational energy barrier due the smaller

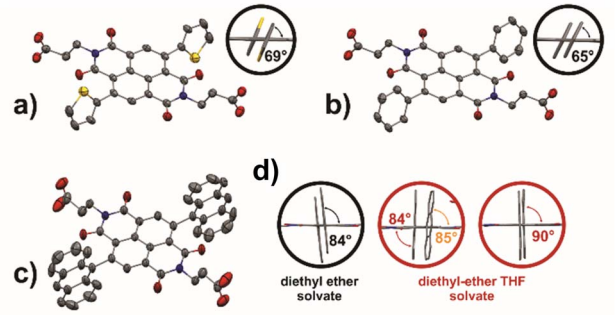

Fig. 3 Single crystal X-ray structures of: (a) **NDI-Th**, (b) **NDI-Ph**, and (c) **NDI-An**. The circular insets highlight the orthogonal structural arrangement of the NDI core and the flanking substituent. The black inset in panel (d) shows the orthogonal structure of **NDI-An** molecules in the diethyl-ether solvate, while the red insets show similar conformations in the two crystallographically independent molecules of the diethyl-ether-THF solvate. All solvent molecules, minor occupancy sites and hydrogen atoms are omitted to enhance clarity of the presentation. The thermal ellipsoids are drawn at the 50% probability level.

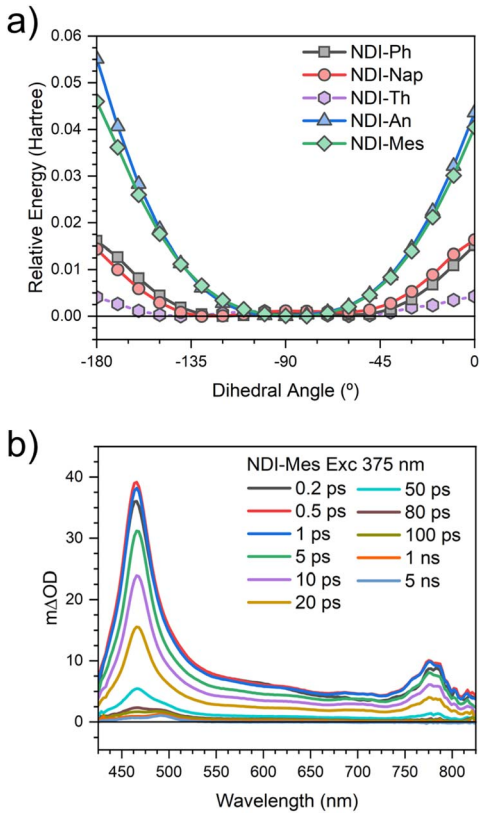

Fig. 4 (a) Unrelaxed potential energy scan modifying the torsional angle between the NDI core and one of the substituents. (b) Transient absorption spectroscopy results of a **NDI-Mes** 2-MeTHF solution upon excitation at 375 nm with a power of 0.25 mW.

size of the thienyl substituent leading to the lowest steric hindrance. This is in stark contrast to **NDI-An** which presents the highest energetic barrier to rotation, due to the significant steric hindrance between the NDI core and the anthracene moiety, largely preventing free rotation (Fig. 4a).

The increase in the oxidation potential, due to larger conjugation of the substituent,[87] and, therefore, the stronger donor character, may emerge as an explanation for more efficient charge formation, either in place of or alongside orthogonality. To rule out this possibility we synthesised an additional NDI molecule with a mesityl group as substituent (**NDI-Mes**, see its spectroscopic analysis in Fig. S5). The mesityl has a considerably lower oxidation potential than anthracene, actually its oxidation potential, directly related with the donor strength, places it below the naphthalene.[64,65] However, despite its lower oxidation potential and a much lower conjugation length it possesses a large steric hindrance (with a similar calculated steric hindrance to **NDI-An**, Fig. 4a).

We have conducted TAS characterisation of this novel molecule under identical conditions to the other four (Fig. 4b and S5). As seen, right upon excitation, only the feature with a band at 480 nm which extends to the NIR, associated previously with charges, appears. This feature decays with a 14 ps lifetime. Interestingly, the **NDI-Mes** charges have a less defined spectrum. We hypothesise that the origin for this less defined spectrum is a lower effective charge separation, *i.e.*, shorter distance between charges, for this state than for **NDI-An**.[35] This is in agreement with the much lower size of the mesityl group in comparison to anthracene which makes the separation of the positive and negative electronic densities less effective. However, in this case, there is a signal originated at large times (over 50 ps) which is assigned to NDI triplet state.[15,24,68] In previously reported systems, such triplets typically originate from the higher-lying local singlet state *via* efficient intersystem crossing (ISC), which can occur in less than 200 fs. In **NDI-Mes**, however, triplet formation does not proceed through ISC from a local state. Instead, it occurs *via* charged species, a mechanism also observed in other NDIs functionalized with amines or imide-substituted group.[15,72] Nevertheless, the ISC efficiency in **NDI-Mes** is notably lower, as evidenced by the significantly weaker triplet signal compared to those earlier examples. This conclusion rests on the reasonable assumption that the relative absorptivity of the excited species in **NDI-Mes** is comparable to that in the previously reported NDI derivatives.

As stated before, the introduction of this mesityl substituted molecule to this work neglects the oxidation potential, as experimental figure of merit for the donor strength, of the substituents as the main origin for the charge generation process (Fig. S7). The use of the pure donor oxidation potential as donor strength character was pertinent since the molecules showed considerable decoupling between the donor and acceptor moieties, as indicated by the CV measurements and calculations. Indeed, the CV revealed only a 50 meV variation in reduction potential across the molecules of greatest interest, which could still introduce some error into the relationship.

Since substituent donor strength was not enough to justify these molecules behaviour, we focused on the substituent orthogonality. To quantify the orthogonality and the charge generation relationship we need a suitable way to assess a charge generation yield. However, the TA spectra reveal no

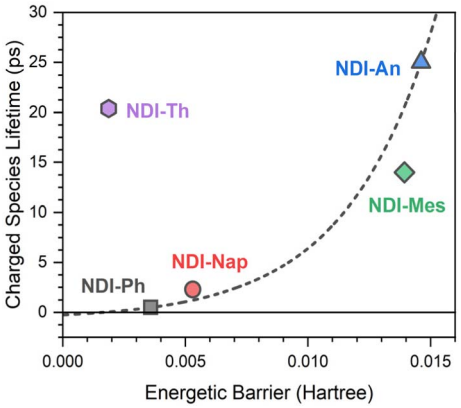

Fig. 5 Relationship between the charge lifetime and the rotational barrier between the NDI core and the substituents of the studied molecules **NDI-Ph** (black square), **NDI-Nap** (red circle), **NDI-An** (blue triangle) and **NDI-Mes** (green diamond). An exponential fitting has been added to help the eye (dashed line). The value for the rotational barrier is the energy difference between the most stable conformation and the molecule with a −30° angle between the core and the substituent.

detectable NDI singlet exciton signal at even the shortest measured delay (200 fs). Given an NDI singlet lifetime of 1 ps (a literature-based conservative estimation for solvent variation),[24,72] at 200 fs, a significant portion of the initial NDI singlet population, calculated to be *ca.* 80%, should still remain. This lack of signal suggests an ultrafast charge generation process, thereby negating its suitability as a comparative metric. Then, we have used the charge lifetime as better approximation to distinguish between them. Still, charge lifetime does not express, by itself, the charge generation yield but it is directly related to the charge stability and is a valuable comparison for application matters. This approximation is particularly valuable for the **NDI-An**, since co-excitation remains an issue to properly characterise the charge generation yield. Fig. 5 shows the relationship between the charge lifetime and the rotational energetic barrier. As seen, there is a correlation between the charge lifetime and the orthogonality. A monotonic increase in the calculated rotational barrier (Fig. 4a) increases the observed charged-state lifetime (Fig. 5), suggesting that restricted rotation may play an important role in stabilizing the CT state.

The **NDI-Th** does not follow the trend as the charge generation process in this molecule is not driven by geometry constraints but rather on electronic effects given by the large donor nature of the thiophene (as explained in the ground state absorbance discussion). The **NDI-Th** results suggest that charge generation in common literature NDI examples are not driven by molecular geometry but by electronic effects by introduction of either a donor or an acceptor atom/group.

We also performed calculations to investigate the relationship between the experimental charge decay rate with the ΔG (Table 1), following Marcus theory formalism (Fig. S8). We have calculated the ΔG as the electronic difference of the minimum of the S_1 (with large CT character in all cases) and the S_0 of truncated derivatives, to optimise the computation time. We estimate that changes in geometry from these two states would be minimal, and, therefore, changes in entropy should be negligible. This ΔG is compared to the experimental charge relaxation rate for all compounds. Performing the calculations in vacuum typically leads to larger reorganisation energies. However, applying the same vacuum conditions to all compounds preserves a consistent systematic error and allows us to isolate the influence of backbone torsion, minimizing any contributions from solvent effects. In this work, the rates follow a trend in the normal region of the Marcus theory with a faster decay rate for a larger $-\Delta G$. To place these observations within the Marcus framework, it is useful to recall that the intramolecular charge-transfer rate depends not only on the free energy and reorganisation energy but also on the electronic coupling. Although the free-energy variations follow the expected trend, they cannot fully explain the large differences in charge relaxation. The geometric orthogonality modulates orbital overlap and thus the electronic coupling, providing a clearer explanation for the charge-distribution efficiency than free-energy changes alone.

As explained in the introduction, to unequivocally unravel the identity of the charges generated in these molecules represents a challenge due to their similarities in terms of spectral properties.[28] The small size of the molecules presented in this work seems to be insufficient to generate a separated charge

Table 1 Experimental and calculated spectroscopic and electrochemical data for the studied molecules

Molecule	Lifetime (ps)[a]	Energetic barrier (Hartree)[b]	Substituent ox. potential (eV)[c]	Calculated $\Delta G°$ (eV)[d]
NDI-Th	20.4	0.00187	1.54[63]	—
NDI-Ph	0.5	0.00358	2.08[65]	−2.057
NDI-Nap	2.3	0.0053	1.34[65]	−1.703
NDI-Mes	14	0.01394	1.55[65]	−1.688
NDI-An	25	0.01461	0.84[65]	−1.010

[a] Decay rate from charged species in TAS. [b] Calculated energetic barrier from unrestricted calculation at 30° between the NDI core and the substituent. [c] Oxidation potentials taken from literature *vs.* Ag/AgCl. These values are also in agreement with potentials under other conditions.[64] [d] Calculation details are provided in SI.

species. However, the **NDI-An** and, to a lesser extent, **NDI-Mes** charges spectra show a larger definition and a slight shift in comparison with **NDI-Ph** and **NDI-Nap** charges. This suggests the formation of a larger effective separation of this CT state if not the formation of separated charges in line with other examples in literature where the difference between the CT and the separated charges are also a slight shift in the spectrum.[28]

The present work about intramolecular charge generation underpins a broad range of applications. Intramolecular charge generation usually constitutes the initial step in photocatalysis, generating the reactive species required for the reaction of interest.[88,89] Efficient charge generation is also central to photovoltaics, where charges must be created and extracted before recombination occurs. This is especially critical in single-component photovoltaics, which avoid the donor:acceptor interfacial recombination that typically limits device performance.[90,91] Furthermore, radicals play an important role in a large number of biological processes, and, hence, a fast radical formation is of great interest in the field of bioapplications.[42,92]

Conclusions

In conclusion, we have studied the implications of torsion-modulated on intramolecular charge generation in NDI molecules, focusing on the steric hindrance with lower donor strength building blocks. The solution study in TAS probes the formation of these charges prior the signal detection limit (hundreds of femtoseconds). A larger rotational barrier of the substituent correlates with longer-lived charged states, since reduced electronic coupling stabilises this species. In addition, the lifetime of the as-created charges is increased with the rotational barrier following an exponential growth, with an R^2 value of 0.885. The introduction of this new recipe for charge generation is the first step in the production of a new family of molecules for single-component devices with better industrial scalability as it does not rely in very complex donor–acceptor design. However, the implications of this new approach for charge generation does not stop here as it has implications for a much broader range of applications from bioapplications, organic electronics to catalysis.

Author contributions

HCB, CL, ABA and LMC have prepared the compounds. AMSD and SG have performed the theoretical calculations. DKB performed the crystallographic measurements and analyses. JMMB has performed the spectroscopic characterisation and analysis. HCB, ABT, BCS, SG and JMMB have elaborated the manuscript. JMMB supervised the project.

Conflicts of interest

There are no conflicts to declare.

Data availability

CCDC 2413777–2413780 contain the supplementary crystallographic data for this paper.[104a–d]

Data for this article, including NMR, UV-vis, PL, psTAS and Raman spectra are available at UCL Research Data Repository at https://doi.org/10.5522/04/28203680. The data supporting this article have been included as part of the supplementary information (SI). The authors have cited additional references within the SI.[93–103] Supplementary information is available. See DOI: https://doi.org/10.1039/d6sc00456c.

Acknowledgements

JMMB wants to acknowledge the Spanish University Ministry and the European Union for his Maria Zambrano fellowship with NextGen-Eu funding and the University of Malaga for the Young Researchers Projects (1-2021_17). JMMB also wants to thank the Research Central Services (SCAI) of the University of Málaga for access to the EVI, EEL, and MENL to perform ground-state and transient spectroscopic characterization. Simulations were performed using the high performance computing resources of the Castilla y León Supercomputing Center (SCAYLE), funded by the European Regional Development Fund (ERDF). AMS thanks the Spanish Ministry of Science and Innovation (MCIN/AEI/10.13039/501100011033) grant no. PID2020-113147GA-I00. SG thanks the EPSRC under the COSMOS programme grant (EP/X026973/1) and the Spanish Ministry of Science and Innovation (MCIN/AEI/10.13039/501100011033) grant PID2024-162002NB-I00. BCS acknowledges funding from the UK Research and Innovation for Future Leaders Fellowship (MR/S031952/1). This work was supported by the CRUK City of London Centre Award (C7893/A26233) and (CTRQQR-2021/100004).

Notes and references

1 J. Nelson, *Phys. Rev. B: Condens. Matter Mater. Phys.*, 2003, **67**, 155209.
2 X. Lan, X. Liu, Y. Zhang, Q. Li, J. Wang, Q. Zhang and G. Bai, *ACS Catal.*, 2021, **11**, 7429–7441.
3 J. Zaumseil, R. H. Friend and H. Sirringhaus, *Nat. Mater.*, 2006, **5**, 69–74.
4 H. B. Naveed and W. Ma, *Joule*, 2018, **2**, 621–641.
5 A. Guerrero and G. Garcia-Belmonte, *Nano–Micro Lett.*, 2017, **9**, 10.
6 M. S. Vezie, M. Azzouzi, A. M. Telford, T. R. Hopper, A. B. Sieval, J. C. Hummelen, K. Fallon, H. Bronstein, T. Kirchartz, A. A. Bakulin, T. M. Clarke and J. Nelson, *ACS Energy Lett.*, 2019, **4**, 2096–2103.
7 D. Baran, R. S. Ashraf, D. A. Hanifi, M. Abdelsamie, N. Gasparini, J. A. Röhr, S. Holliday, A. Wadsworth, S. Lockett, M. Neophytou, C. J. M. Emmott, J. Nelson, C. J. Brabec, A. Amassian, A. Salleo, T. Kirchartz, J. R. Durrant and I. McCulloch, *Nat. Mater.*, 2017, **16**, 363–369.

8 J. Hamonnet, M. Nakano, K. Nakano, H. Sugino, K. Takimiya and K. Tajima, *Chem. Mater.*, 2017, **29**, 9618–9622.
9 E. Ahmed, G. Ren, F. S. Kim, E. C. Hollenbeck and S. A. Jenekhe, *Chem. Mater.*, 2011, **23**, 4563–4577.
10 N. Zhou and A. Facchetti, *Mater. Today*, 2018, **21**, 377–390.
11 J. H. Oh, S. Suraru, W. Lee, M. Könemann, H. W. Höffken, C. Röger, R. Schmidt, Y. Chung, W. Chen, F. Würthner and Z. Bao, *Adv. Funct. Mater.*, 2010, **20**, 2148–2156.
12 B. A. Jones, A. Facchetti, T. J. Marks and M. R. Wasielewski, *Chem. Mater.*, 2007, **19**, 2703–2705.
13 B. J. Jung, K. Lee, J. Sun, A. G. Andreou and H. E. Katz, *Adv. Funct. Mater.*, 2010, **20**, 2930–2944.
14 N. T. La Porte, J. A. Christensen, M. D. Krzyaniak, B. K. Rugg and M. R. Wasielewski, *J. Phys. Chem. B*, 2019, **123**, 7731–7739.
15 X. Chen, A. A. Sukhanov, M. Taddei, B. Dick, J. Zhao, V. K. Voronkova and M. Di Donato, *J. Phys. Chem. Lett.*, 2022, **13**, 8740–8748.
16 S. Chakraborty, D. Ray, V. K. Aswal and S. Ghosh, *Chem.–Eur. J.*, 2018, **24**, 16379–16387.
17 M. K. Gish, A. L. Jones, J. M. Papanikolas and K. S. Schanze, *J. Phys. Chem. C*, 2018, **122**, 18802–18808.
18 K. Cai, J. Xie, X. Yang and D. Zhao, *Org. Lett.*, 2014, **16**, 1852–1855.
19 K. Cai, J. Xie and D. Zhao, *J. Am. Chem. Soc.*, 2014, **136**, 28–31.
20 K. Kranthiraja, D. X. Long, V. G. Sree, W. Cho, Y.-R. Cho, A. Zaheer, J.-C. Lee, Y.-Y. Noh and S.-H. Jin, *Macromolecules*, 2018, **51**, 5530–5536.
21 Y. Zhao, X. Li, Z. Wang, W. Yang, K. Chen, J. Zhao and G. G. Gurzadyan, *J. Phys. Chem. C*, 2018, **122**, 3756–3772.
22 P. Pahlavanlu, A. J. Tilley, B. T. McAllister and D. S. Seferos, *J. Org. Chem.*, 2017, **82**, 12337–12345.
23 K. Chen, J. Zhao, X. Li and G. G. Gurzadyan, *J. Phys. Chem. A*, 2019, **123**, 2503–2516.
24 O. Yushchenko, G. Licari, S. Mosquera-Vazquez, N. Sakai, S. Matile and E. Vauthey, *J. Phys. Chem. Lett.*, 2015, **6**, 2096–2100.
25 J. Shaikh, D. G. Congrave, A. Forster, A. Minotto, F. Cacialli, T. J. H. Hele, T. J. Penfold, H. Bronstein and T. M. Clarke, *Chem. Sci.*, 2021, **12**, 8165–8177.
26 S. Kasemthaveechok, L. Abella, M. Jean, M. Cordier, T. Roisnel, N. Vanthuyne, T. Guizouarn, O. Cador, J. Autschbach, J. Crassous and L. Favereau, *J. Am. Chem. Soc.*, 2020, **142**, 20409–20418.
27 Y. Wu, S. Schneider, Y. Yuan, R. M. Young, T. Francese, I. F. Mansoor, P. J. Dudenas, Y. Lei, E. D. Gomez, D. M. DeLongchamp, M. C. Lipke, G. Galli, M. R. Wasielewski, J. B. Asbury, M. F. Toney and Z. Bao, *Adv. Energy Mater.*, 2022, **12**, 2103957.
28 G. J. Moore, F. Günther, K. M. Yallum, M. Causa', A. Jungbluth, J. Réhault, M. Riede, F. Ortmann and N. Banerji, *Nat. Commun.*, 2024, **15**, 9851.
29 H. Langhals, S. Kinzel and A. Obermeier, *J. Org. Chem.*, 2024, **89**, 2138–2154.
30 A. M. El-Zohry, E. A. Orabi, M. Karlsson and B. Zietz, *J. Phys. Chem. A*, 2021, **125**, 2885–2894.
31 Y. Yao, P. Ding, C. Yan, Y. Tao, B. Peng, W. Liu, J. Wang, M. A. Cohen Stuart and Z. Guo, *Angew. Chem., Int. Ed.*, 2023, **62**, e202218983.
32 E. Wang, J. W. Y. Lam, R. Hu, C. Zhang, Y. S. Zhao and B. Z. Tang, *J. Mater. Chem. C*, 2014, **2**, 1801.
33 M. A. Haidekker and E. A. Theodorakis, *Org. Biomol. Chem.*, 2007, **5**, 1669–1678.
34 J. M. Marin-Beloqui, D. G. Congrave, D. T. W. Toolan, S. Montanaro, J. Guo, I. A. Wright, T. M. Clarke, H. Bronstein and S. D. Dimitrov, *J. Am. Chem. Soc.*, 2023, **145**, 3507–3514.
35 J. M. Marin-Beloqui, K. J. Fallon, H. Bronstein and T. M. Clarke, *J. Phys. Chem. Lett.*, 2019, **10**, 3813–3819.
36 J. Marin-Beloqui, G. Zhang, J. Guo, J. Shaikh, T. Wohrer, S. M. Hosseini, B. Sun, J. Shipp, A. J. Auty, D. Chekulaev, J. Ye, Y.-C. Chin, M. B. Sullivan, A. J. Mozer, J.-S. Kim, S. Shoaee and T. M. Clarke, *J. Phys. Chem. C*, 2022, **126**, 2708–2719.
37 T. M. Clarke, A. Ballantyne, S. Shoaee, Y. W. Soon, W. Duffy, M. Heeney, I. McCulloch, J. Nelson and J. R. Durrant, *Adv. Mater.*, 2010, **22**, 5287–5291.
38 C. G. Shuttle, B. O'Regan, A. M. Ballantyne, J. Nelson, D. D. C. Bradley and J. R. Durrant, *Phys. Rev. B: Condens. Matter Mater. Phys.*, 2008, **78**, 113201.
39 E. Busby, J. Xia, Q. Wu, J. Z. Low, R. Song, J. R. Miller, X.-Y. Zhu, L. M. Campos and M. Y. Sfeir, *Nat. Mater.*, 2015, **14**, 426–433.
40 J. S. Ward, R. S. Nobuyasu, A. S. Batsanov, P. Data, A. P. Monkman, F. B. Dias and M. R. Bryce, *Chem. Commun.*, 2016, **52**, 2612–2615.
41 S. D. Dimitrov, S. Wheeler, D. Niedzialek, B. C. Schroeder, H. Utzat, J. M. Frost, J. Yao, A. Gillett, P. S. Tuladhar, I. McCulloch, J. Nelson and J. R. Durrant, *Nat. Commun.*, 2015, **6**, 6501.
42 X. Cui, Z. Zhang, Y. Yang, S. Li and C. Lee, *Exploration*, 2022, **2**, 20210264.
43 A. Sarkar, T. Behera, R. Sasmal, R. Capelli, C. Empereur-mot, J. Mahato, S. S. Agasti, G. M. Pavan, A. Chowdhury and S. J. George, *J. Am. Chem. Soc.*, 2020, **142**, 11528–11539.
44 A. Sarkar, R. Sasmal, A. Das, A. Venugopal, S. S. Agasti and S. J. George, *Angew. Chem., Int. Ed.*, 2021, **60**, 18209–18216.
45 M. Sasikumar, Y. V. Suseela and T. Govindaraju, *Asian J. Org. Chem.*, 2013, **2**, 779–785.
46 T. A. Welsh, O. Matsarskaia, R. Schweins and E. R. Draper, *New J. Chem.*, 2021, **45**, 14005–14013.
47 X. Chen, Y. He, M. U. Ali, Y. He, Y. Zhu, A. Li, C. Zhao, I. F. Perepichka and H. Meng, *Sci. China Chem.*, 2019, **62**, 1360–1364.
48 B. Reiß and H.-A. Wagenknecht, *Beilstein J. Org. Chem.*, 2019, **15**, 2043–2051.
49 K. Sonogashira, Y. Tohda and N. Hagihara, *Tetrahedron Lett.*, 1975, **16**, 4467–4470.
50 N. Miyaura, K. Yamada and A. Suzuki, *Tetrahedron Lett.*, 1979, **20**, 3437–3440.

51 M. Frigoli, M. Caldara, J. Royakkers, J. W. Lowdon, T. J. Cleij, H. Diliën, K. Eersels and B. van Grinsven, *Microchem. J.*, 2024, **200**, 110433.
52 J. Royakkers, K. Guo, D. T. W. Toolan, L. Feng, A. Minotto, D. G. Congrave, M. Danowska, W. Zeng, A. D. Bond, M. Al-Hashimi, T. J. Marks, A. Facchetti, F. Cacialli and H. Bronstein, *Angew. Chem., Int. Ed.*, 2021, **60**, 25005–25012.
53 P. Piyakulawat, A. Keawprajak, A. Chindaduang, M. Hanusch and U. Asawapirom, *Synth. Met.*, 2009, **159**, 467–472.
54 J. K. Stille, *Angew Chem. Int. Ed. Engl.*, 1986, **25**, 508–524.
55 P. Espinet and A. M. Echavarren, *Angew. Chem., Int. Ed.*, 2004, **43**, 4704–4734.
56 S. Kuila, A. Ghorai, P. K. Samanta, R. B. K. Siram, S. K. Pati, K. S. Narayan and S. J. George, *Chem.–Eur. J.*, 2019, **25**, 16007–16011.
57 H. A. M. van Mullekom, J. A. J. M. Vekemans and E. W. Meijer, *Chem.–Eur. J.*, 1998, **4**, 1235–1243.
58 B. Grimm, C. Risko, J. D. Azoulay, J.-L. Brédas and G. C. Bazan, *Chem. Sci.*, 2013, **4**, 1807.
59 L. Pandey, C. Risko, J. E. Norton and J.-L. Brédas, *Macromolecules*, 2012, **45**, 6405–6414.
60 Y. S. Rosokha, S. V. Lindeman, S. V. Rosokha and J. K. Kochi, *Angew. Chem., Int. Ed.*, 2004, **43**, 4650–4652.
61 H. T. Chifotides, B. L. Schottel and K. R. Dunbar, *Angew. Chem., Int. Ed.*, 2010, **49**, 7202–7207.
62 B. Han, J. Lu and J. K. Kochi, *Cryst. Growth Des.*, 2008, **8**, 1327–1334.
63 M. B. Camarada, P. Jaque, F. R. Díaz and M. A. del Valle, *J. Polym. Sci., Part B: Polym. Phys.*, 2011, **49**, 1723–1733.
64 L. Eberson and K. Nyberg, *J. Am. Chem. Soc.*, 1966, **88**, 1686–1691.
65 W. C. Neikam and M. M. Desmond, *J. Am. Chem. Soc.*, 1964, **86**, 4811–4814.
66 S. B. Schmidt, T. Biskup, X. Jiao, C. R. McNeill and M. Sommer, *J. Mater. Chem. C*, 2019, **7**, 4466–4474.
67 S. V. Rosokha and J. K. Kochi, in *Halogen Bonding*, Springer Berlin Heidelberg, Berlin, Heidelberg, pp. , pp. 137–160.
68 A. Aster, C. Rumble, A.-B. Bornhof, H.-H. Huang, N. Sakai, T. Šolomek, S. Matile and E. Vauthey, *Chem. Sci.*, 2021, **12**, 4908–4915.
69 D. Gosztola, M. P. Niemczyk, W. Svec, A. S. Lukas and M. R. Wasielewski, *J. Phys. Chem. A*, 2000, **104**, 6545–6551.
70 J. Sepioł, *J. Lumin.*, 1986, **36**, 115–120.
71 B. Manna, R. Ghosh and D. K. Palit, *J. Phys. Chem. C*, 2015, **119**, 10641–10652.
72 P. Ganesan, J. Baggerman, H. Zhang, E. J. R. Sudhölter and H. Zuilhof, *J. Phys. Chem. A*, 2007, **111**, 6151–6156.
73 A. Singh, L. Weatherill, A. Agarwal, S. M, C. Tonnele, D. Casanova, R. Singh, F. Dias and I. Laskar, *ChemRxiv*, 2025, preprint, DOI: 10.26434/chemrxiv-2025-pgpn8.
74 K. Wang, X. You, X. Miao, Y. Yi, S. Peng, D. Wu, X. Chen, J. Xu, M. Y. Sfeir and J. Xia, *J. Am. Chem. Soc.*, 2024, **146**, 13326–13335.
75 M. E. El-Khouly, C. A. Wijesinghe, V. N. Nesterov, M. E. Zandler, S. Fukuzumi and F. D'Souza, *Chem.–Eur. J.*, 2012, **18**, 13844–13853.
76 Y. Mori, Y. Sakaguchi and H. Hayashi, *J. Phys. Chem. A*, 2002, **106**, 4453–4467.
77 M. P. Debreczeny, W. A. Svec, E. M. Marsh and M. R. Wasielewski, *J. Am. Chem. Soc.*, 1996, **118**, 8174–8175.
78 S. Ito, T. Nagami and M. Nakano, *J. Phys. Chem. A*, 2016, **120**, 6236–6241.
79 E. W. Castner, D. Kennedy and R. J. Cave, *J. Phys. Chem. A*, 2000, **104**, 2869–2885.
80 Y. Hou, I. Kurganskii, A. Elmali, H. Zhang, Y. Gao, L. Lv, J. Zhao, A. Karatay, L. Luo and M. Fedin, *J. Chem. Phys.*, 2020, **152**, 114701.
81 F. Neese, *Wiley Interdiscip. Rev. Comput. Mol. Sci.*, 2012, **2**, 73–78.
82 Y. Shao, Z. Gan, E. Epifanovsky, A. T. B. Gilbert, M. Wormit, J. Kussmann, A. W. Lange, A. Behn, J. Deng, X. Feng, D. Ghosh, M. Goldey, P. R. Horn, L. D. Jacobson, I. Kaliman, R. Z. Khaliullin, T. Kuś, A. Landau, J. Liu, E. I. Proynov, Y. M. Rhee, R. M. Richard, M. A. Rohrdanz, R. P. Steele, E. J. Sundstrom, H. L. Woodcock, P. M. Zimmerman, D. Zuev, B. Albrecht, E. Alguire, B. Austin, G. J. O. Beran, Y. A. Bernard, E. Berquist, K. Brandhorst, K. B. Bravaya, S. T. Brown, D. Casanova, C.-M. Chang, Y. Chen, S. H. Chien, K. D. Closser, D. L. Crittenden, M. Diedenhofen, R. A. DiStasio, H. Do, A. D. Dutoi, R. G. Edgar, S. Fatehi, L. Fusti-Molnar, A. Ghysels, A. Golubeva-Zadorozhnaya, J. Gomes, M. W. D. Hanson-Heine, P. H. P. Harbach, A. W. Hauser, E. G. Hohenstein, Z. C. Holden, T.-C. Jagau, H. Ji, B. Kaduk, K. Khistyaev, J. Kim, J. Kim, R. A. King, P. Klunzinger, D. Kosenkov, T. Kowalczyk, C. M. Krauter, K. U. Lao, A. D. Laurent, K. V. Lawler, S. V. Levchenko, C. Y. Lin, F. Liu, E. Livshits, R. C. Lochan, A. Luenser, P. Manohar, S. F. Manzer, S.-P. Mao, N. Mardirossian, A. V. Marenich, S. A. Maurer, N. J. Mayhall, E. Neuscamman, C. M. Oana, R. Olivares-Amaya, D. P. O'Neill, J. A. Parkhill, T. M. Perrine, R. Peverati, A. Prociuk, D. R. Rehn, E. Rosta, N. J. Russ, S. M. Sharada, S. Sharma, D. W. Small, A. Sodt, T. Stein, D. Stück, Y.-C. Su, A. J. W. Thom, T. Tsuchimochi, V. Vanovschi, L. Vogt, O. Vydrov, T. Wang, M. A. Watson, J. Wenzel, A. White, C. F. Williams, J. Yang, S. Yeganeh, S. R. Yost, Z.-Q. You, I. Y. Zhang, X. Zhang, Y. Zhao, B. R. Brooks, G. K. L. Chan, D. M. Chipman, C. J. Cramer, W. A. Goddard, M. S. Gordon, W. J. Hehre, A. Klamt, H. F. Schaefer, M. W. Schmidt, C. D. Sherrill, D. G. Truhlar, A. Warshel, X. Xu, A. Aspuru-Guzik, R. Baer, A. T. Bell, N. A. Besley, J.-D. Chai, A. Dreuw, B. D. Dunietz, T. R. Furlani, S. R. Gwaltney, C.-P. Hsu, Y. Jung, J. Kong, D. S. Lambrecht, W. Liang, C. Ochsenfeld, V. A. Rassolov, L. V. Slipchenko, J. E. Subotnik, T. Van Voorhis, J. M. Herbert, A. I. Krylov, P. M. W. Gill and M. Head-Gordon, *Mol. Phys.*, 2015, **113**, 184–215.
83 H. Wang and M. Thoss, *J. Chem. Phys.*, 2003, **119**, 1289–1299.
84 G. A. Worth, *Comput. Phys. Commun.*, 2020, **248**, 107040.

85 H. Köuppel, W. Domcke and L. S. Cederbaum, Multimode Molecular Dynamics Beyond the Born-Oppenheimer Approximation, in *Advances in Chemical Physics*, ed. I. Prigogine and S.A. Rice, 1984, pp. 59–246.
86 A. Martín Santa Daría, L. González-Sánchez and S. Gómez, *Phys. Chem. Chem. Phys.*, 2024, **26**, 174–184.
87 J. L. Bredas, R. Silbey, D. S. Boudreaux and R. R. Chance, *J. Am. Chem. Soc.*, 1983, **105**, 6555–6559.
88 M. Fumanal, A. Ortega-Guerrero, K. M. Jablonka, B. Smit and I. Tavernelli, *Adv. Funct. Mater.*, 2020, **30**, 2003792.
89 F. Chen, T. Ma, T. Zhang, Y. Zhang and H. Huang, *Adv. Mater.*, 2021, **33**, 2005256.
90 S. M. Menke, N. A. Ran, G. C. Bazan and R. H. Friend, *Joule*, 2018, **2**, 25–35.
91 H. B. Naveed, K. Zhou and W. Ma, *Acc. Chem. Res.*, 2019, **52**, 2904–2915.
92 J. Liu, M. Wu, R. Zhang and Z. P. Xu, *View*, 2021, **2**, 20200139.
93 A. C. Thompson, H. M. Grimm, A. Gray Bé, K. J. McKnight and J. J. Reczek, *Synth. Commun.*, 2015, **45**, 1127–1136.
94 Y. Yu, J. Wang, Y. Cui, Z. Chen, T. Zhang, Y. Xiao, W. Wang, J. Wang, X.-T. Hao and J. Hou, *J. Am. Chem. Soc.*, 2024, **146**, 8697–8705.
95 P. Tang, T. Furuya and T. Ritter, *J. Am. Chem. Soc.*, 2010, **132**, 12150–12154.
96 Y. Chen, M. Chen and Y. Liu, *Angew. Chem., Int. Ed.*, 2012, **51**, 6181–6186.
97 N. N. Sergeeva, A. Scala, M. A. Bakar, G. O'Riordan, J. O'Brien, G. Grassi and M. O. Senge, *J. Org. Chem.*, 2009, **74**, 7140–7147.
98 *CrysAllisPro 1.171.42.60a*, Rigaku, 2022.
99 G. M. Sheldrick, *Acta Crystallogr., Sect. A: Found. Adv.*, 2015, **71**, 3–8.
100 O. V. Dolomanov, L. J. Bourhis, R. J. Gildea, J. A. K. Howard and H. Puschmann, *J. Appl. Crystallogr.*, 2009, **42**, 339–341.
101 G. M. Sheldrick, *Acta Crystallogr., Sect. C: Struct. Chem.*, 2015, **71**, 3–8.
102 C. B. Hübschle, G. M. Sheldrick and B. Dittrich, *J. Appl. Crystallogr.*, 2011, **44**, 1281–1284.
103 B. Rees, L. Jenner and M. Yusupov, *Acta Crystallogr., Sect. D: Biol. Crystallogr.*, 2005, **61**, 1299–1301.
104 (*a*) CCDC 2413777: Experimental Crystal Structure Determination, 2026, DOI: 10.5517/ccdc.csd.cc2m0qs5; (*b*) CCDC 2413778: Experimental Crystal Structure Determination, 2026, DOI: 10.5517/ccdc.csd.cc2m0qt6; (*c*) CCDC 2413779: Experimental Crystal Structure Determination, 2026, DOI: 10.5517/ccdc.csd.cc2m0qv7; (*d*) CCDC 2413780: Experimental Crystal Structure Determination, 2026, DOI: 10.5517/ccdc.csd.cc2m0qw8.